

Localized spin-orbit polaron in magnetic Weyl semimetal $\text{Co}_3\text{Sn}_2\text{S}_2$

Yuqing Xing^{1,2,3†}, Jianlei Shen^{1,2†}, Hui Chen^{1,2,3†}, Yuxiang Gao^{1,2,3}, Yu-Yang Zhang^{2,3}, Geng Li^{1,2,3}, Bin Hu^{1,2,3}, Guojian Qian^{1,2,3}, Xianli Zhang^{1,2,3}, Peng Fan^{1,2,3}, Qi Wang⁴, Qiangwei Yin⁴, Hechang Lei⁴, Wei Ji⁴, Shixuan Du^{1,2,3,5}, Haitao Yang^{1,2,3}, Chengmin Shen^{1,2,3}, Enke Liu^{1,2,5}, Baogen Shen^{1,2}, Ziqiang Wang^{6*}, and Hong-Jun Gao^{1,2,3,5*}*

¹ *Beijing National Center for Condensed Matter Physics and Institute of Physics, Chinese Academy of Sciences, Beijing 100190, PR China*

² *School of Physical Sciences, University of Chinese Academy of Sciences, Beijing 100190, PR China*

³ *CAS Center for Excellence in Topological Quantum Computation, University of Chinese Academy of Sciences, Beijing 100190, PR China*

⁴ *Beijing Key Laboratory of Optoelectronic Functional Materials & Micro-Nano Devices, Department of Physics, Renmin University of China, Beijing 100872, PR China*

⁵ *Songshan Lake Materials Laboratory, Dongguan, Guangdong 523808, PR China*

⁶ *Department of Physics, Boston College, Chestnut Hill, MA, USA*

†These authors contributed equally to this work

*Correspondence to: hjgao@iphy.ac.cn, wangzi@bc.edu, ekliu@iphy.ac.cn

As a magnetic Weyl semimetal¹⁻⁴, $\text{Co}_3\text{Sn}_2\text{S}_2$ integrates the flat bands of correlated d -electrons on the kagome lattice^{5,6} into the topological band structure⁷⁻¹⁰ and exhibits remarkable properties such as the giant anomalous Hall/Nernst effect^{7,11}, chiral-anomaly⁷, surface-termination dependent Fermi arcs¹⁰, topological catalysis¹², flat band Berry phase and orbital magnetism¹³. Probing the nature of the magnetism in $\text{Co}_3\text{Sn}_2\text{S}_2$ is thus crucial for understanding the physical origin, implications, as well as the control of the emergent novel phenomena through manipulation of magnetic order. Here, using spin-polarized scanning tunneling microscopy/spectroscopy (STM/S) combined with first-principle calculations, we study the layer-resolved magnetic behaviors and localized spin-orbit polaron in magnetic Weyl semimetal $\text{Co}_3\text{Sn}_2\text{S}_2$. We find that the Sn-terminated surface has a nonzero spin-polarization antiparallel to that of the Co_3Sn layer, while the S-terminated surface is nonmagnetic. On the S-terminated surface, we observe bound magnetic polarons localized around single-S vacancies with a three-fold rotation symmetry, a polarization antiparallel to the magnetization of the Sn surface, and formed out of the correlated d -electron orbitals in the Co_3Sn plane. Studying their response to external magnetic field up to ± 6 T reveals an anomalous Zeeman effect, indicating a dominant orbital contribution, in contrast to bound magnetic polarons in dilute magnetic semiconductors. We term this new excitation as a bound spin-orbit polaron (SOP). Our findings suggest that engineering of single-S atomic vacancies in S-deficient $\text{Co}_3\text{Sn}_2\text{S}_{2-\delta}$ may offer a new direction to enhance magnetism in a controlled fashion through the bound SOP.

$\text{Co}_3\text{Sn}_2\text{S}_2$ has a layered structure which consists of two hexagonal planes of S and Sn as well as a Co_3Sn kagome layer sandwiched between them (Fig. 1a-b). As previous literature reported, the Curie temperature of such compound is at 177 K and the spontaneous magnetic moment is about $0.3 \mu_{\text{B}}/\text{Co}$ ^{8,14,15}. Single crystals of $\text{Co}_3\text{Sn}_2\text{S}_2$ were cleaved in-situ at 6 K under ultrahigh-vacuum and immediately transferred to the STM head. Weak bonds between S and Sn atoms offer a cleave plane and lead to S-terminated (top in Fig. 1b) and Sn-terminated surface (middle in Fig. 1b). In topographic STM images, S-terminated surfaces show a hexagonal lattice with some randomly distributed vacancies (Fig. 1d), while Sn-terminated surfaces show a similar hexagonal lattice with adatoms and clusters (Fig. 1f). The dI/dV spectra on these two surfaces measured using a tungsten tip (Extended Data Fig. 1) are in good agreement with previous reports^{10,16,17}.

In order to study the magnetism of $\text{Co}_3\text{Sn}_2\text{S}_2$, we carried out spin-polarized measurements on S and Sn terminated surfaces with a ferromagnetic (FM) Ni tip, as schematically shown in Fig. 1c. The spin-polarization of the Ni tip was calibrated on Co/Cu(111) (Extended Data Fig. 2). External magnetic fields of +0.6 T (-0.6 T) were applied to magnetize the Ni tip to be in the spin up (spin down) states. This tip was then used to measure the spin-dependent dI/dV spectra at 0 T. In the defect-free regions of the S terminated surface, we did not observe spin-polarized contrast, indicating that the intact S-terminated surface is non-magnetic (Fig. 1e). On the Sn surface, however, the dI/dV spectrum taken with the spin-up tip shows much stronger intensity than that taken with the spin-down tip (Fig. 1g), indicating the presence of an FM order in the Sn layer.

To understand the distinct response of the two surfaces with different atomic terminations to spin-polarized tunneling, we carried out DFT calculations of the electronic structures of $\text{Co}_3\text{Sn}_2\text{S}_2$. The spin-resolved, projected density of states (PDOS) on the S-terminated surface (Extended Data Fig. 1) shows that the two spin channels are almost degenerate. The net magnetic moment in the S layer is nearly zero. For the Sn-terminated surface, however, the calculated PDOS shows significant spin-polarization (Extended Data Fig. 1) with a net magnetic moment of $0.04 \mu_B$. These results are consistent with our STM/S measurements. Moreover, the DFT calculations show that the FM moment in the Sn layer is antiparallel to that ($0.3 \mu_B$) of a Co atom in the Co_3Sn layer, which show the same magnetic order as that in the bulk material (Extended Data Method part). The STM/S together with the DFT results reveals the layer-resolved magnetic structure: a dominant FM ordered Co_3Sn layer, a weaker FM Sn layer with opposite magnetization, and a nonmagnetic S layer. Thus, the FM $\text{Co}_3\text{Sn}_2\text{S}_2$ is in fact a weak ferrimagnet.

We next study the properties of localized excitations by focusing on a region with S vacancies on the S-terminated surface (Fig. 2). An atomic topographic image shows two single-S vacancies labeled as A and B, as well as a vacancy-dimer C (Fig. 2a). A typical dI/dV spectrum taken off of vacancies resembles closely that taken in a clean region on the S-surface far away, exhibiting an energy gap of 300meV (black curve in Fig. 2b)^{10,16}. In particular, the dI/dV map of the broad hump around +50 meV (Fig. 2c), which is believed to originate from the topological surface states of the magnetic Weyl semimetal^{10,16}, shows extended states with weakened intensity at the S-vacancies. Similarly, the peak near the top of the valence band at -350 meV has a spatial distribution seen in the dI/dV map (Fig. 2d) with suppressed density of states around the S-vacancy sites. Remarkably, the dI/dV spectrum taken at the site of vacancy A (red circle in Fig. 2a) reveals a series of approximately equal-spaced spectral peaks just above the valence band top (orange curve in Fig. 2b), indicative of S-vacancy induced in-gap bound states. To elucidate the spatial

structure of the bound states, we measured dI/dV maps (Fig. 2e, 2f, and 2g) at -322, -300, and -280 meV, corresponding to the three discernable peaks. The bound states are localized and have a flower petal shaped pattern with a three-fold rotation symmetry around the single-S vacancies A and B. The electrons scatter from the S-vacancy potential and form a bound state corresponding to the sharp primary peak \sim -280 meV much like a localized polaron, and the higher order peaks can be understood as due to the polaron shake-off process. These features at the single-S vacancies are highly reproducible in different regions and on different samples (Extended Data Fig. 3). From the statistical analysis, we determine the average spacing between the spectral peaks to be \sim 16meV (Extended Data Fig. 3).

To investigate the magnetic properties of the bound states, we switch to spin-polarized Ni tip and obtain the dI/dV spectra on a single-S vacancy D (Fig. 3a). The strong magnetic contrast over the energy range from -350 to -270 meV shows that the bound states are magnetic with a spin-down majority. The spin flip operation of the Ni tip is shown in Fig. 3b, where we zoom in to one of the two sub-peaks associated with the primary bound state, possibly due to the exchange field induced energy splitting (Extended Data Fig. 4). A spin down- tip was initially prepared, which gave a pronounced bound state peak around -283 meV (left panel in Fig. 3b). The polarization of the tip was then flipped to spin-up by an external magnetic field of +0.6 T. The intensity of the peak at -283 meV was reduced while the peak position did not change (middle panel in Fig. 3b). After flipping the tip back to spin-down, the peak intensity increases back to the initial level (right panel in Fig. 3b). These demonstrate the excellent reproducibility of the spin flip operation^{18,19}, and that the bound states are magnetic polarons introduced by the S vacancies. Interestingly, the magnetization of all bound magnetic polarons is opposite to the FM moment in the Sn layer, but in the same direction as the ordered moment in the Co₃-Sn layer. Indeed, from the high resolution dI/dV map acquired with the W tip around vacancy D (Fig. 3c), the three-fold symmetric spatial profile of the bound magnetic polaron can be traced out and superimposed onto the atomic structure projected to the S-surface (Fig. 3d), revealing its overall correlation with the underlying Co atoms. These experimental findings are qualitatively in agreement with and supported by our DFT calculations (Extended Data Fig. 5).

To further investigate the nature of the bound magnetic polaron, we measure the magnetic field response of the spectral peaks in dI/dV using a normal W tip. The magnetic field is applied perpendicular to the sample surface, ranging from -6 T to 6 T. As shown in Fig. 4a and b, when the amplitude of the magnetic field increases, the peak positions shift linearly toward the higher energy side, *independent of the direction of the magnetic field*. Such an anomalous Zeeman response is reproducible on different vacancies

(Extended Data Fig. 6), and indicates the important orbital contribution to the magnetic moment of the polaron. Because of this, we will refer to the polaron as a bound spin-orbit polaron (SOP). By fitting the two peak positions as a function of the magnetic field (Fig. 4c), we obtained a slope of $75 \mu\text{eV/T} = 1.35 \mu_B$ for the effective moment of the SOP. We have also measured the magnetic field dependence of the near-zero-energy peak on the Sn-terminated surface, and observed a similar anomalous shift (Extended Data Fig. 7), which was attributed to the Berry phase induced orbital magnetization in the kagome flat band¹³. It is remarkable that the bound SOP nucleated at the S vacancies in $\text{Co}_3\text{Sn}_2\text{S}_2$ presents a localized analog of the anomalous Zeeman shift, highlighting the rich and novel behaviors of the correlated and topological d -electrons in this kagome-lattice Weyl semimetal.

Finally, we study the magnetic-lattice coupling of the bound SOP. The lattice distortion around the S vacancies (Fig. 4d) shows significant local atomic displacements (see also Extended Data Fig. 8). To quantify the lattice distortion, we measure the average nearest atom distance around the S vacancy and determine the local atomic displacement ratio as its percentage changes from the average nearest atom distance far away from the vacancy. The local atomic displacement ratio is $\sim 6\%$ under zero magnetic field. An external magnetic field is then applied along the c -axis. We find the local atomic displacement ratio decreases significantly with increasing magnetic field strength (Extended Data Fig. 9), and about one-third of the displacement ratio can be manipulated by a magnetic field up to 6 T. These observations further support the SOP nature of the S vacancy-induced bound states and the strong magnetic-lattice coupling in $\text{Co}_3\text{Sn}_2\text{S}_2$.

We have revealed the intriguing and diverse magnetism in $\text{Co}_3\text{Sn}_2\text{S}_2$ with both itinerant and localized contributions. The main findings are summarized in the schematic illustration (Fig. 4e). The itinerant FM order is weakly ferrimagnetic with oppositely polarized magnetic moments in the Co_3Sn and the Sn layers, while the S surface is nonmagnetic. Such layer-dependent magnetism may be relevant for the recently observed diversity in the Fermi arc topological surface states¹⁰. The missing S atom causes strong scattering and hybridization between the p -electrons of S and the d -electrons of the underlying Co, giving rise to a localized bound SOP with antiparallel (parallel) magnetization direction as compared to that of the Sn (Co_3Sn) surface. Bound magnetic polarons play an important role in dilute magnetic semiconductors^{20–22}, where they form around the doped magnetic impurity ions and order magnetically through the Ruderman–Kittel–Kasuya–Yosida (RKKY) interactions. The bound SOP at the vacancies in the nonmagnetic layer discovered here is new and open a direction for manipulating the magnetic order

in the Weyl semimetal $\text{Co}_3\text{Sn}_2\text{S}_2$. While it is currently unclear the extent to which S vacancies exist in as grown stoichiometric materials, S deficient $\text{Co}_3\text{Sn}_2\text{S}_{2-\delta}$ crystals have been synthesized²³ and should allow controlled and systematic study of the magnetism as a function of the density of the S vacancies. The bound SOP should emerge and enhance the saturated ordered moment as observed recently at small S deficiency²³. We propose that increasing the SOP density will raise the Curie temperature and enable topological properties, such as the giant anomalous Hall and Nernst transport, to be observed at higher temperatures.

Methods

Single crystal growth of $\text{Co}_3\text{Sn}_2\text{S}_2$

The single crystals of $\text{Co}_3\text{Sn}_2\text{S}_2$ were grown by flux method with Sn/Pb mixed flux. The starting materials of Co (99.95% Alfa), Sn (99.999% Alfa), S (99.999% Alfa) and Pb (99.999% Alfa) were mixed in molar ratio of Co : S : Sn : Pb = 12 : 8 : 35 : 45. The mixtures were placed in Al_2O_3 crucibles sealed in quartz tubes. The quartz tubes were slowly heated to 673 K over 6 h and kept there over 6 h to avoid the heavy loss of sulfur. The quartz tubes were further heated to 1323 K over 6 h and left there for 6 h. Then the melt was cooled down slowly to 973 K over 70 h. At 973 K, the flux was removed by rapid decanting and subsequent spinning in a centrifuge. The hexagonal-plate single crystals with diameters of 2 ~ 5 mm were obtained. The compositions and phase structure of the crystals were checked by energy-dispersive x-ray spectroscopy and x-ray diffraction, respectively.

Scanning tunneling microscope and spectroscopy

The samples used in the experiments were cleaved *in situ* at 6 K and immediately transferred to an STM head. Experiments were performed in an ultrahigh vacuum (1×10^{-10} mbar) ULT-STM systems (40 mK) equipped with 9-2-2 T magnetic field. All the scanning parameter (setpoint voltage and current) of the STM topographic images are listed in the captions of the figures. Unless otherwise noted, the differential conductance (dI/dV) spectra were acquired by a standard lock-in amplifier at a frequency of 973.1 Hz. Non-magnetic tungsten tip was fabricated via electrochemical etching and calibrated on a clean Au(111) surface prepared by repeated cycles of sputtering with argon ions and annealing at 500 °C. Ferromagnetic Ni tips were applied in the spin-polarized STM measurement. The Ni tips were fabricated via electrochemical etching of Ni wires in a constant-current mode²⁸. To calibrate the spin-polarization of Ni tip, the prepared Ni tips have been applied to resolve magnetic-state-dependent contrast of Co islands grown on a Cu(111) surface in SP-STM experiments (details are shown in Extended Data Fig. 2).

Density functional theory

Quantum mechanical calculations based on density functional theory (DFT) were performed by using the_Vienna Ab initio Simulation Package (VASP)^{24,25}. The projector augmented wave (PAW)²⁶ method

was employed, and the Perdew–Burke–Ernzerhof (PBE)²⁷ type of exchange correlation functional was used.

The slab models containing six Co-Sn layers and extra S or Sn layers were used to simulate the S-terminated and Sn-terminated surfaces. S surfaces with a single S vacancy were simulated by a 4×4 supercell. In structural relaxations, the atoms in the two middle Co₃Sn layers were fixed, while atoms in other layers were totally relaxed. The vacuum layers of the slab models are larger than 15 Å.

The wavefunctions are expanded in plane waves with a kinetic energy cutoff of 400 eV. For pristine S-terminated and Sn-terminated surfaces of Co₃Sn₂S₂, the k-points sampling is 8×8×1, generated by Monkhorst-Pack grids with the origin at the Γ -point. The structures were relaxed until the energy and residual force on each atom were smaller than 10⁻⁶ eV and 0.001 eV/Å, respectively. For S-terminated surface with single vacancy, the k-points sampling is with only the Γ -point. The structures were relaxed until the energy and residual force on each atom were smaller than 10⁻⁴ eV and 0.01 eV/Å, respectively. With these parameters, the optimized lattice constant of bulk Co₃Sn₂S₂ is 5.37 Å and 13.15 Å for a and c directions, respectively. The magnetic moment is -0.35 μ_B , 0.02 μ_B , 0.03 μ_B , and 0 μ_B for Co, Sn in Co₃Sn plan, Sn in Sn layer, and S, respectively.

References

1. Wang, Z. *et al.* Time-reversal-breaking Weyl fermions in magnetic Heusler alloys. *Phys. Rev. Lett.* **117**, 236401 (2016).
2. Xu, G., Weng, H., Wang, Z., Dai, X. & Fang, Z. Chern semimetal and the quantized anomalous Hall effect in HgCr_2Se_4 . *Phys. Rev. Lett.* **107**, 186806 (2011).
3. Burkov, A. A. & Balents, L. Weyl semimetal in a topological insulator multilayer. *Phys. Rev. Lett.* **107**, 127205 (2011).
4. Wan, X., Turner, A. M., Vishwanath, A. & Savrasov, S. Y. Topological semimetal and Fermi-arc surface states in the electronic structure of pyrochlore iridates. *Phys. Rev. B* **83**, 205101 (2011).
5. Ye, L. *et al.* Massive Dirac fermions in a ferromagnetic kagome metal. *Nature* **555**, 638–642 (2018).
6. Yin, J.-X. *et al.* Giant and anisotropic many-body spin–orbit tunability in a strongly correlated kagome magnet. *Nature* **562**, 91–95 (2018).
7. Liu, E. *et al.* Giant anomalous Hall effect in a ferromagnetic kagome-lattice semimetal. *Nat. Phys.* **14**, 1125–1131 (2018).
8. Wang, Q. *et al.* Large intrinsic anomalous Hall effect in half-metallic ferromagnet $\text{Co}_3\text{Sn}_2\text{S}_2$ with magnetic Weyl fermions. *Nat. Commun.* **9**, 3681 (2018).
9. Liu, D. F. *et al.* Magnetic Weyl semimetal phase in a Kagomé crystal. *Science* **365**, 1282–1285 (2019).
10. Morali, N. *et al.* Fermi-arc diversity on surface terminations of the magnetic Weyl semimetal $\text{Co}_3\text{Sn}_2\text{S}_2$. *Science* **365**, 1286–1291 (2019).
11. Guin, S. N. *et al.* Zero-field Nernst effect in a ferromagnetic kagome-lattice Weyl-semimetal $\text{Co}_3\text{Sn}_2\text{S}_2$. *Adv. Mater.* **31**, 1806622 (2019).
12. Li, G. *et al.* Surface states in bulk single crystal of topological semimetal $\text{Co}_3\text{Sn}_2\text{S}_2$ toward water oxidation. *Sci. Adv.* **5**, eaaw9867 (2019).
13. Yin, J.-X. *et al.* Negative flat band magnetism in a spin–orbit-coupled correlated kagome magnet. *Nat. Phys.* **15**, 443–448 (2019).
14. Kubodera, T., Okabe, H., Kamihara, Y. & Matoba, M. Ni substitution effect on magnetic and transport properties in metallic ferromagnet. *Physica B: Condensed Matter* **378–380**, 1142–1143 (2006).
15. Schnelle, W. *et al.* Ferromagnetic ordering and half-metallic state of $\text{Sn}_2\text{Co}_3\text{S}_2$ with the shandite-type structure. *Phys. Rev. B* **88**, 144404 (2013).
16. Jiao, L. *et al.* Signatures for half-metallicity and nontrivial surface states in the kagome lattice Weyl semimetal $\text{Co}_3\text{Sn}_2\text{S}_2$. *Phys. Rev. B* **99**, 245158 (2019).
17. Howard, S. *et al.* Observation of linearly dispersive edge modes in a magnetic Weyl semimetal $\text{Co}_3\text{Sn}_2\text{S}_2$. Preprint at: <https://arxiv.org/abs/1910.11205> (2019).
18. Oka, H. *et al.* Spin-polarized quantum confinement in nanostructures: Scanning tunneling microscopy. *Rev. Mod. Phys.* **86**, 1127–1168 (2014).
19. Chen, W. *et al.* Direct observation of van der Waals stacking–dependent interlayer magnetism. *Science* **366**, 983–987 (2019).
20. Wolff, P. A., Bhatt, R. N. & Durst, A. C. Polaron-polaron interactions in diluted magnetic semiconductors. *J. Appl. Phys.* **79**, 5196 (1996).
21. Kaminski, A. & Das Sarma, S. Polaron percolation in diluted magnetic semiconductors. *Phys. Rev. Lett.* **88**, 247202 (2002).

22. He, M. *et al.* Polaronic transport and magnetism in Ag-doped ZnO. *Appl. Phys. Lett.* **99**, 222511 (2011).
23. Sakai, Y. *et al.* Magnetic properties of shandite-phase $\text{Co}_{3-x}\text{Fe}_x\text{Sn}_2\text{S}_2$ ($x = 0-1.0$) obtained with high pressure synthesis. *J. Phys. Soc. Jpn.* **84**, 044705 (2015).

Figure 1

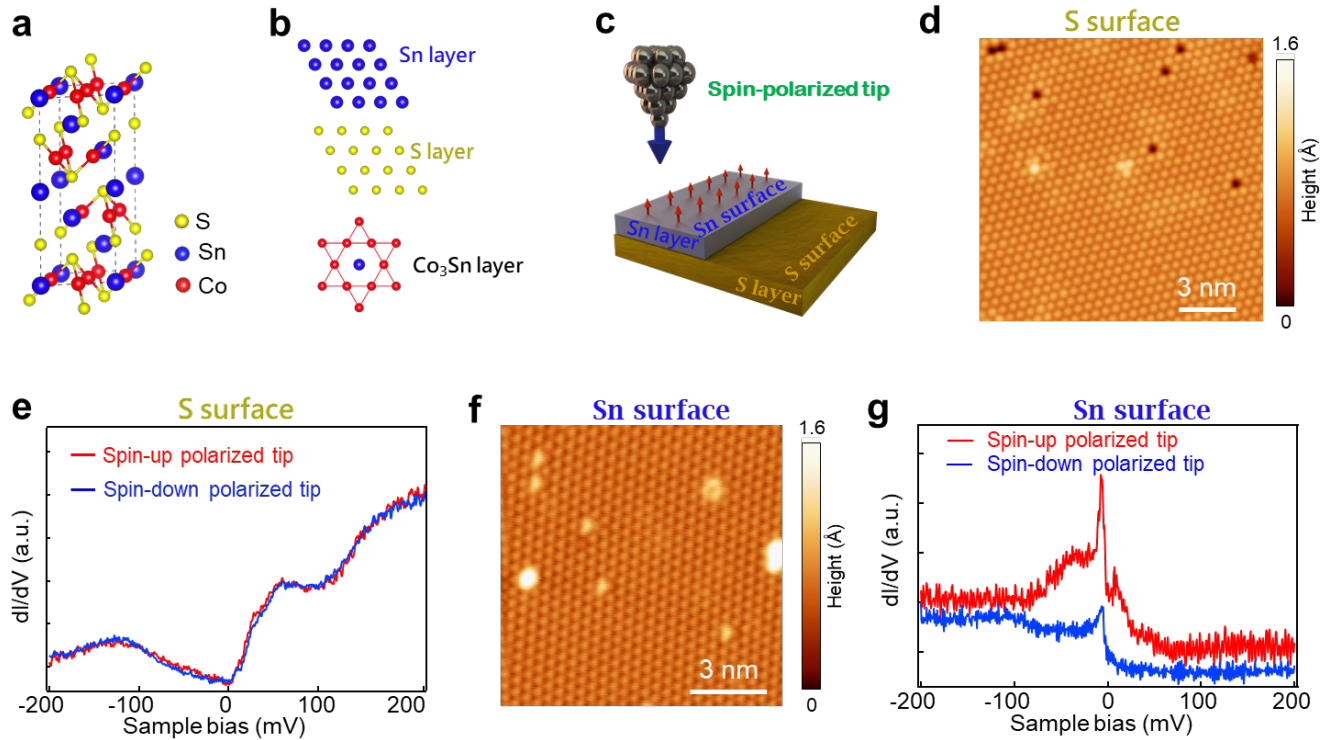


Fig. 1 | Layer-resolved magnetism on S and Sn surface using spin-polarized tip. **a**, Atomic structure of $\text{Co}_3\text{Sn}_2\text{S}_2$. **b**, Atomic structure of S terminated layer, Sn terminated layer and Co_3Sn kagome layer. **c**, Schematic of spin-polarized measurement on distinct terminated surface by using a ferromagnetic Ni tip. **d**, $15 \text{ nm} \times 15 \text{ nm}$ atomic-resolution STM image of the S terminated surface, showing randomly distributed single S vacancies (Scanning setting: bias: $V_s = -400 \text{ mV}$, setpoint $I_t = 100 \text{ pA}$). **e**, dI/dV spectra at intact S surface region using up-polarized tip (red curve) and down-polarized tip (blue curve), showing no polarization contrast on intact S surface ($V_s = -400 \text{ mV}$, $I_t = 100 \text{ pA}$, Modulation $V_{mod} = 0.5 \text{ mV}$). **f**, atomic-resolution STM image of the Sn-terminated surface ($V_s = -400 \text{ mV}$, $I_t = 100 \text{ pA}$). **g**, Spin-polarized dI/dV spectra at Sn surface, showing a more massive intensity of spin-up contribution ($V_s = -400 \text{ mV}$, $I_t = 100 \text{ pA}$, $V_{mod} = 0.5 \text{ mV}$).

Figure 2

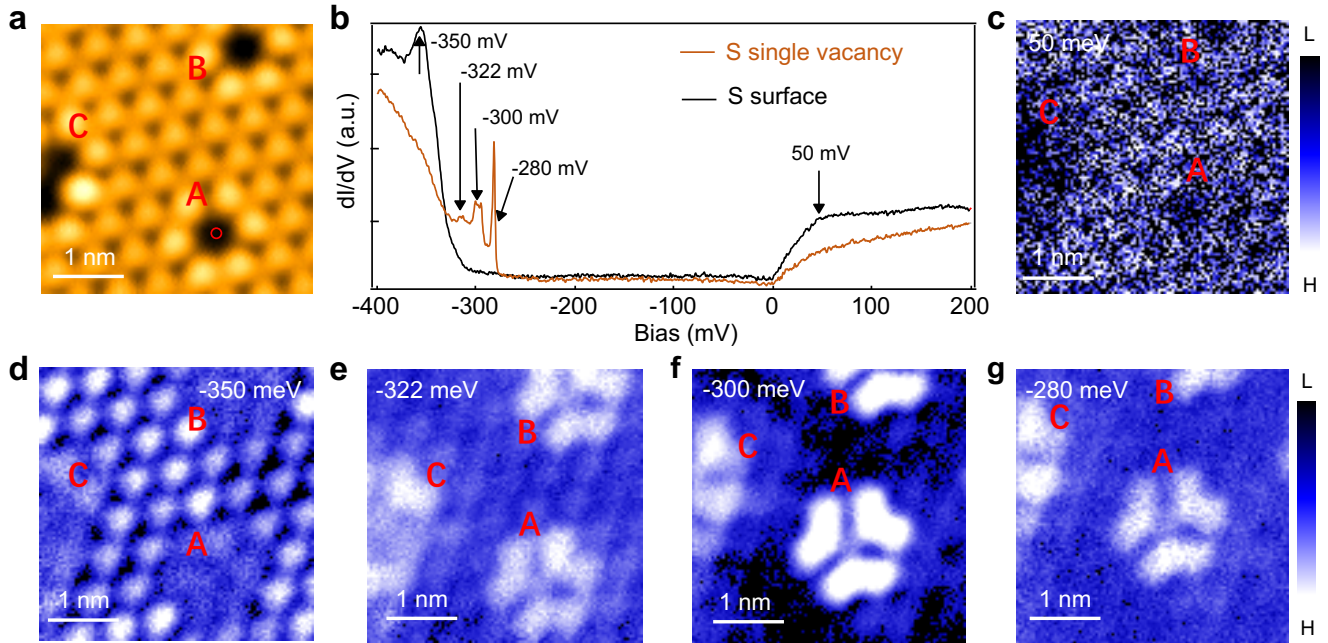


Fig. 2 | Atomic resolved dI/dV map of a single S vacancy. **a**, Topographic image of S vacancy ($V_s = -400$ mV, $I_t = 500$ pA), including two single-S vacancies and one dimer-S vacancy labeled as **A**, **B**, and **C**, respectively. **b**, dI/dV spectra at a single S vacancy (orange curve) and S surface (black curve) ($V_s = -400$ mV, $I_t = 500$ pA, $V_{mod} = 0.5$ mV). **c-g**, dI/dV maps of the region in **(a)** at different energies: 50 meV **(c)**, -350 meV **(d)**, -322 meV **(e)**, -300 meV **(f)**, and -280 meV **(g)**, respectively ($V_s = -400$ mV, $I_t = 500$ pA, $V_{mod} = 0.5$ mV).

Figure 3

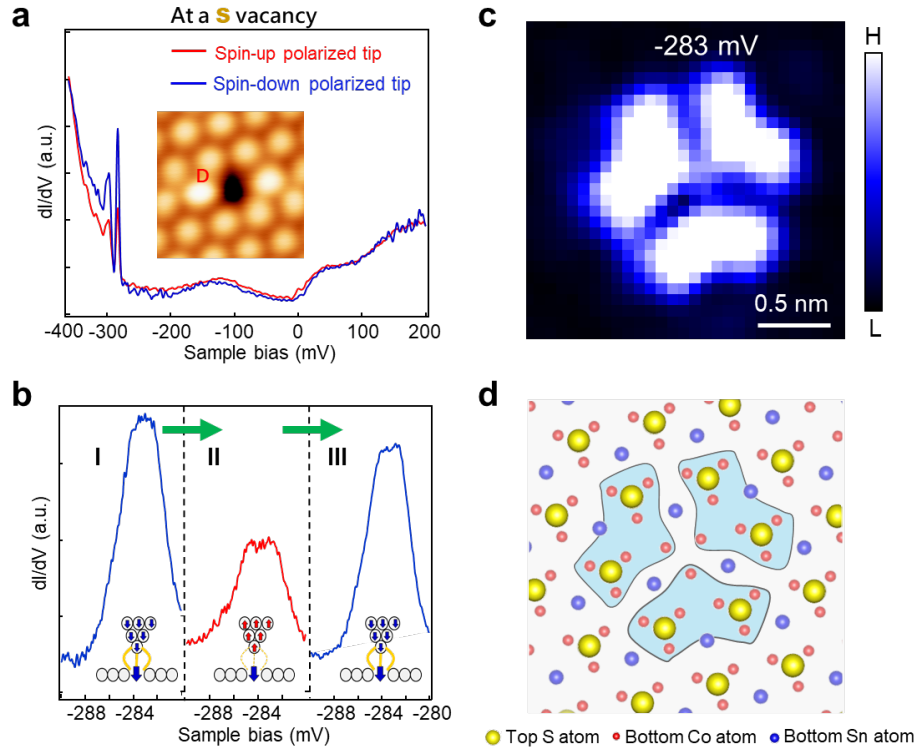


Fig. 3 | Spin-polarized bound states at a single S-vacancy. **a**, dI/dV spectra obtained at the center of a single S vacancy using the Ni STM tip, showing a spin-down majority behavior. The inset shows the topographic image (2 nm x 2 nm) of the single S vacancy ($V_s = -400$ mV, $I_t = 200$ pA, $V_{mod} = 0.5$ mV). **b**, Spin-flip operation of the STM tip and the reproducible spectra at the S vacancy by using the spin-down and spin-up polarized tip. Left curve (curve I) is at the initial spin-down polarization, the middle one (curve II) is of spin-up polarization, and the right (curve III) is in the spin-down polarization. The strong contrast between the spin-down and spin-up polarization measurement and the good match between the initial and final spin-down polarization measurements show the excellent reproducibility of the operation ($V_s = -400$ mV, $I_t = 500$ pA, $V_{mod} = 0.5$ mV). **c**, dI/dV mapping of the inset of (a) at -283 mV, showing that the bound states are localized around the vacancy ($V_s = -400$ mV, $I_t = 500$ pA, $V_{mod} = 0.5$ mV). **d**, Correlation between the atomic structure and the pattern in dI/dV map in (c), showing that the spatial distribution of bound states is correlated to the underlying Co atoms.

Figure 4

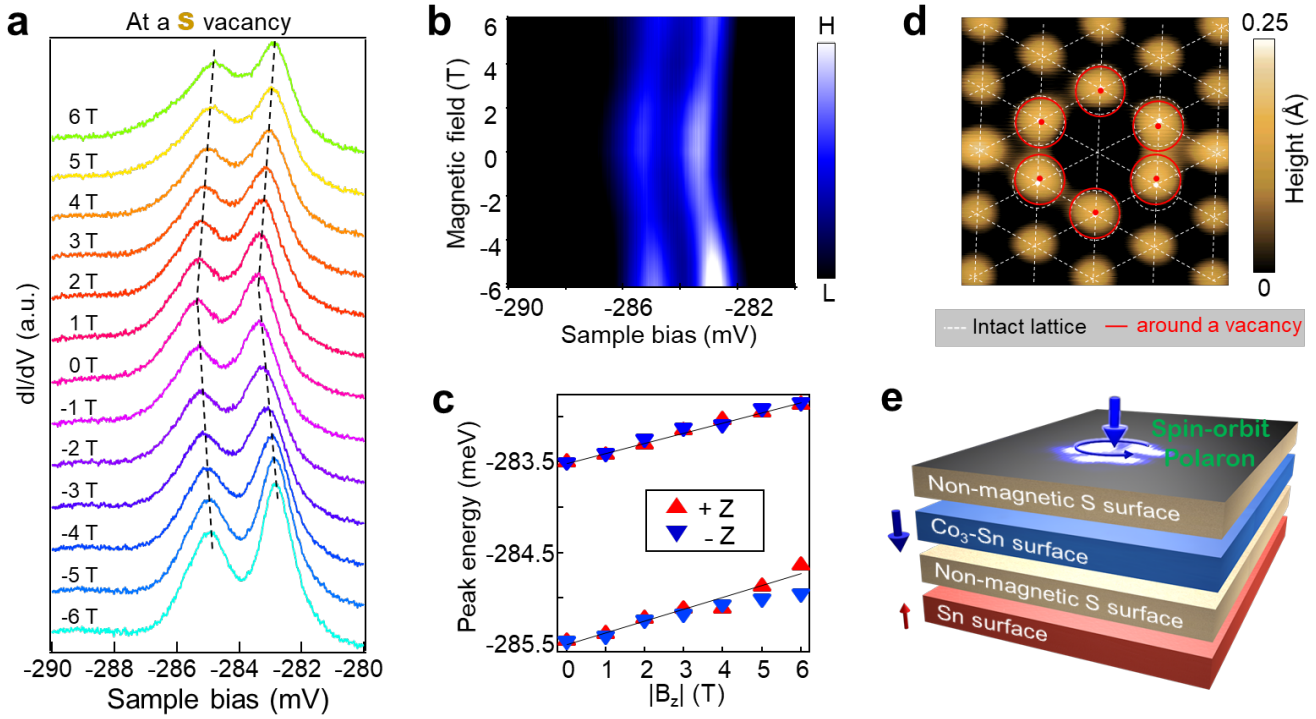


Fig. 4 | Spin-orbit polaron at single S vacancy site. **a**, dI/dV spectra of the bound states with magnetic-field from -6 T to 6 T, showing a linear shift of the bound states under the magnetic field perpendicular to the S surface ($V_s = -400$ mV, $I_t = 500$ pA, $V_{mod} = 0.5$ mV). **b**, Intensity plot of (a), showing a similar shift as in (a). **c**, Energy shift of peak positions as a function of the absolute value of magnetic field. **d**, Lattice distortion around single S vacancy (scale: $2 \text{ nm} \times 2 \text{ nm}$) by comparing the undistorted lattice sites and the intact atoms outlined by white dashed lines to the distorted atomic sites highlighted by the red circles and dots ($V_s = -400$ mV, $I_t = 100$ pA). **e**, Schematic of the layer-dependent magnetism and the localized spin-orbit polaron of $\text{Co}_3\text{Sn}_2\text{S}_2$.

Extended Data Figures and Tables for

Localized spin-orbit polaron in magnetic Weyl semimetal $\text{Co}_3\text{Sn}_2\text{S}_2$

Yuqing Xing^{1,2,3†}, Jianlei Shen^{1,2†}, Hui Chen^{1,2,3†}, Yuxiang Gao^{1,2,3}, Yu-Yang Zhang^{2,3}, Geng Li^{1,2,3}, Bin Hu^{1,2,3}, Guojian Qian^{1,2,3}, Xianli Zhang^{1,2,3†}, Peng Fan^{1,2,3†}, Qi Wang⁴, Qiangwei Yin⁴, Hechang Lei⁴, Wei Ji⁴, Shixuan Du^{1,2,3}, Haitao Yang^{1,2,3}, Chengmin Shen^{1,2,3}, Enke Liu^{1,2,5*}, Baogen Shen^{1,2}, Ziqiang Wang^{6*}, and Hong-Jun Gao^{1,2,3,5*}

¹ Beijing National Center for Condensed Matter Physics and Institute of Physics, Chinese Academy of Sciences, Beijing 100190, PR China

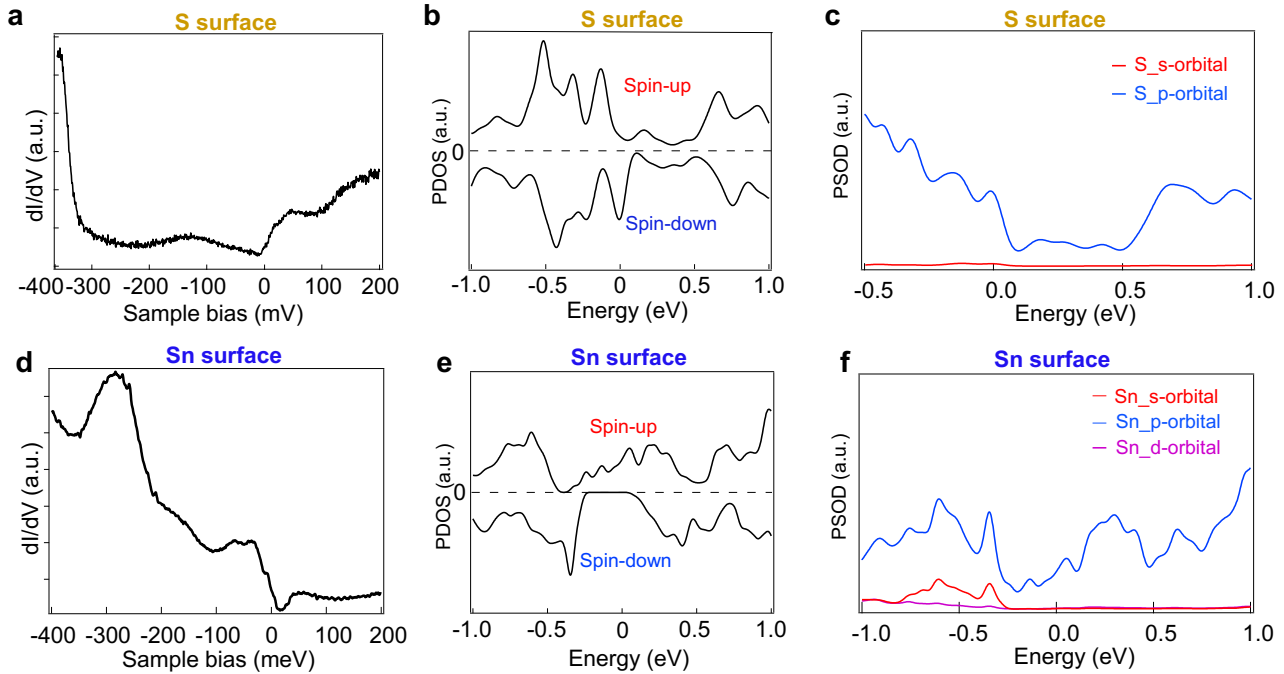
² School of Physical Sciences, University of Chinese Academy of Sciences, Beijing 100190, PR China

³ CAS Center for Excellence in Topological Quantum Computation, University of Chinese Academy of Sciences, Beijing 100190, PR China

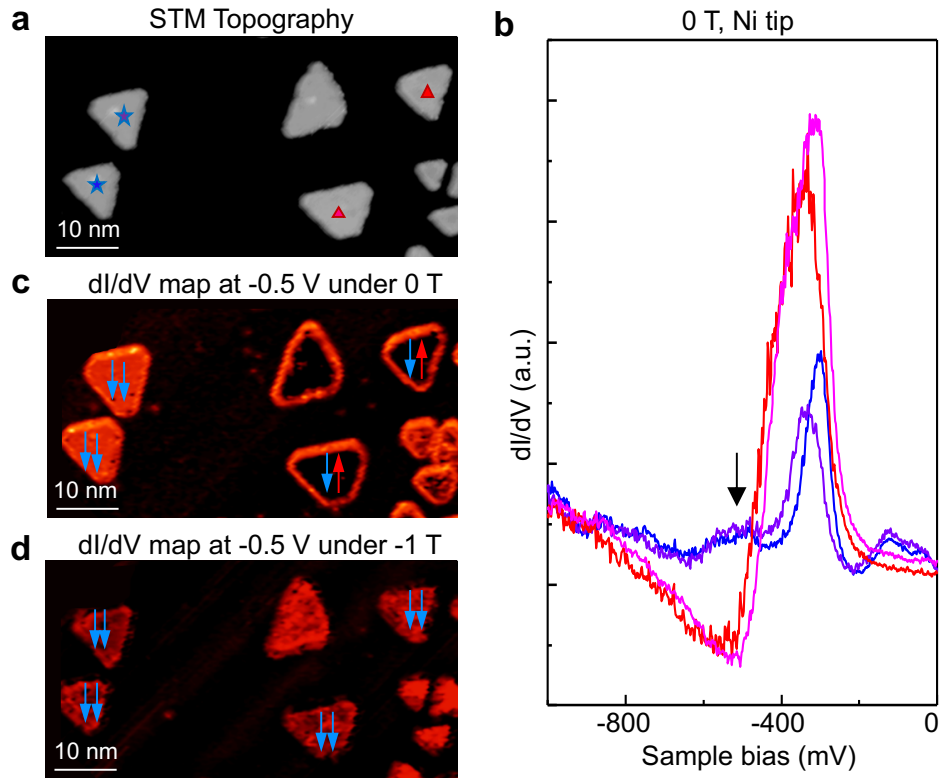
⁴ Beijing Key Laboratory of Optoelectronic Functional Materials & Micro-Nano Devices, Department of Physics, Renmin University of China, Beijing 100872, PR China

⁵ Songshan Lake Materials Laboratory, Dongguan, Guangdong 523808, PR China

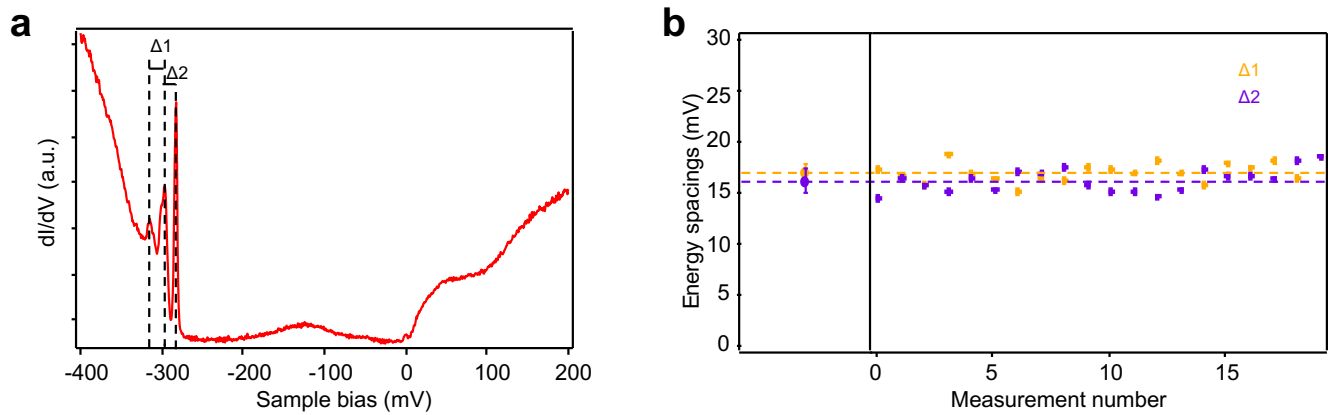
⁶ Department of Physics, Boston College, Chestnut Hill, MA, USA



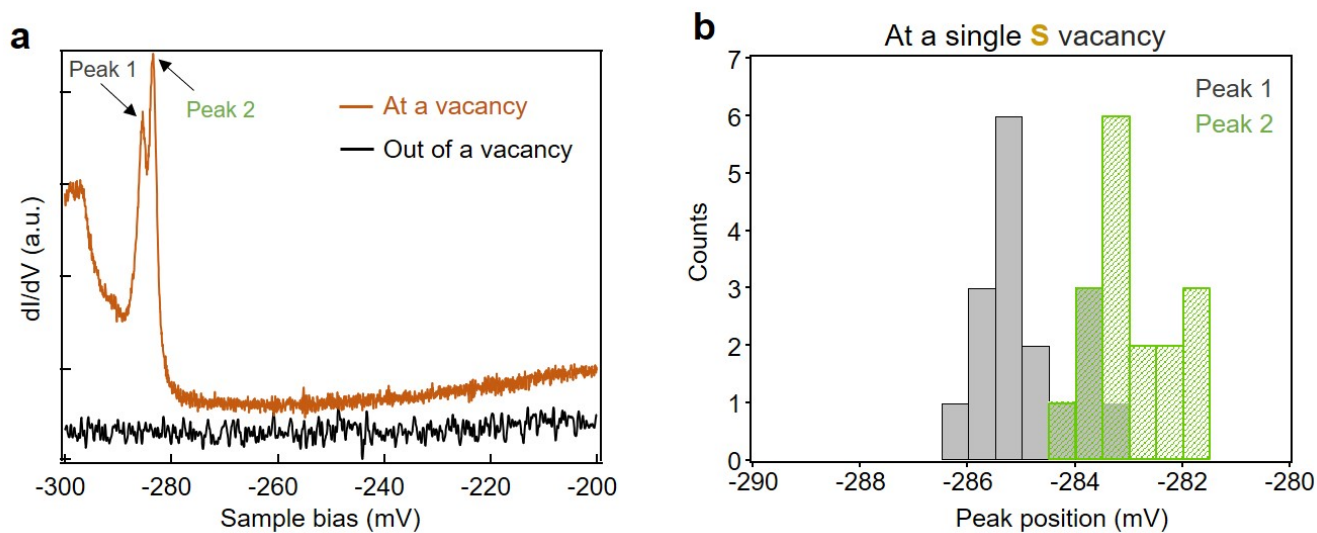
Extended Data Fig. 1 | Surface determination via dI/dV spectra. **a**, The dI/dV spectrum at S-terminated surface ranging from -400 mV to 200 mV. **b**, The spin-resolved density of state (DOS) projected on the surface S atom of the S-terminated surface. The two spin channels do not show significant difference. The net magnetic moment of the surface S atom is almost zero. **c**, The DOS of the surface S atom projected on different orbitals. It is clearly shown that the p-orbital of S is the major contribution. **d**, The dI/dV spectrum at Sn-terminated surface of the same range. **e**, The spin resolved DOS projected on the surface Sn atom of the Sn-terminated surface. It shows a big different between the two spin channels. The net magnetic moment of the surface Sn atom is $0.04 \mu_B$, which is slightly larger than the magnetic moment of Sn atom in bulk ($0.03 \mu_B$). **f**, The DOS of the surface Sn atom. It is also clearly shown that the p-orbital of Sn is the major contribution. dI/dV setting of **(a)** and **(d)**: ($V_s = -400$ mV, $I_t = 200$ pA, $V_{mod} = 0.5$ mV).



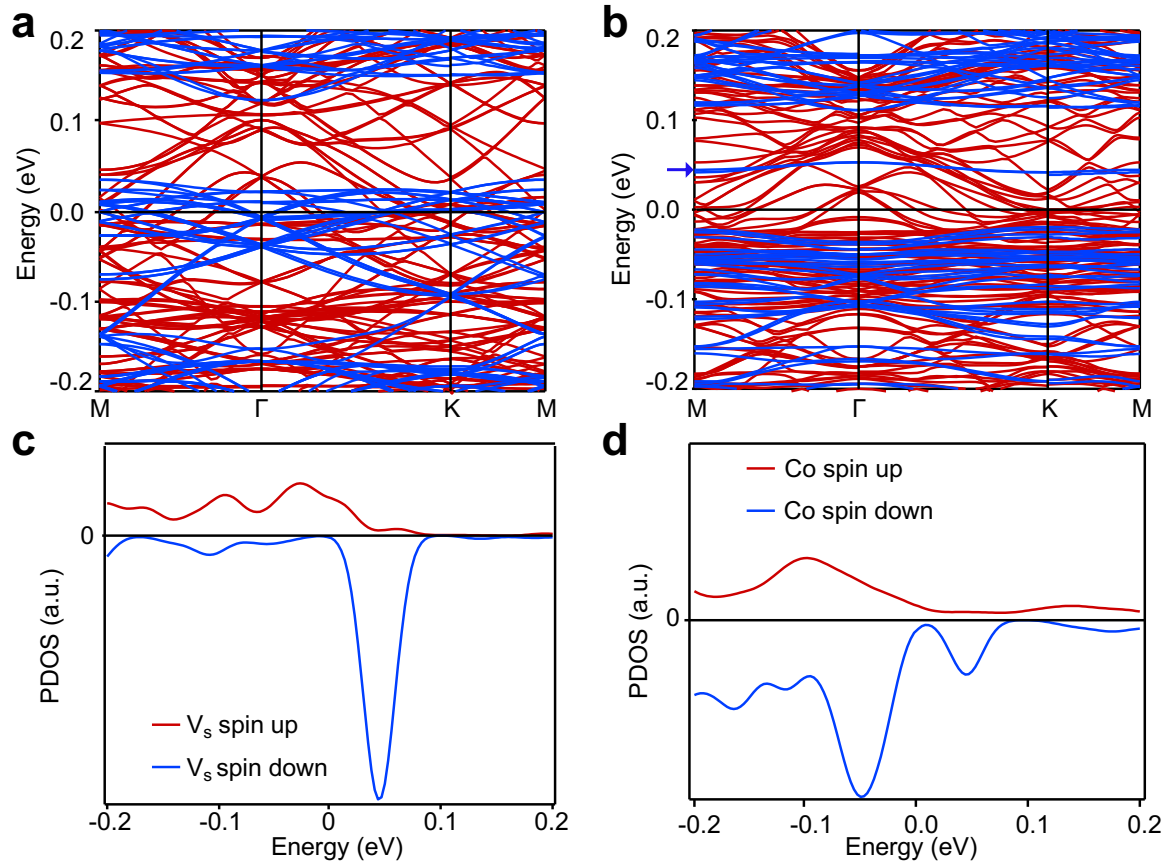
Extended Data Fig. 2 | Calibration of spin-polarized Ni tip on Co/Cu(111). **a**, STM image, showing the topography of Co islands on Cu(111). ($V_s = -400$ mV, $I_t = 100$ pA). **b**, dI/dV spectra obtained on four Co islands with the same stack configurations using the Ni tip. The blue and purple curves are obtained on the blue and purple stars in (a), the pink and red curve are obtained on pink and red triangles in (a). **c-d**, dI/dV mapping of (a) at the energy of -0.5 V at magnetic field of 0 T (c) and -1 T (d). The contrast on the same stacked islands at 0 T and absence of contrast at -1 T confirmed the spin-polarization of Ni tip (detailed please see the reference²⁸). The spin orientation of Co island and tip are labelled by the upward (red) or downward (blue) arrows.



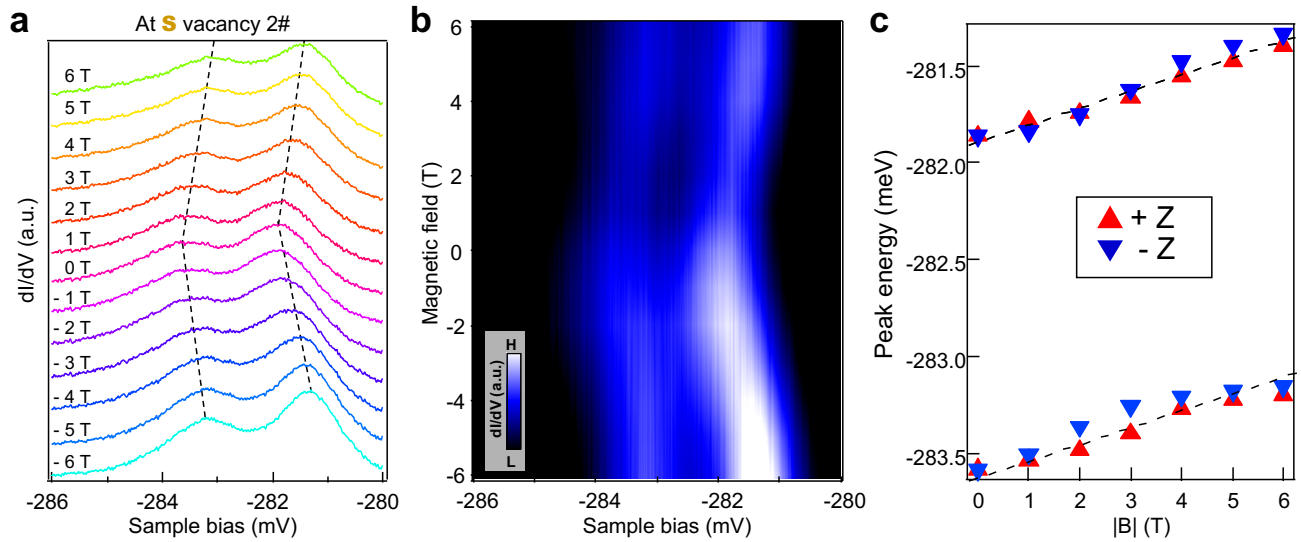
Extended Data Fig. 3 | Energy spacing of the bound states. **a**, Typical dI/dV spectra obtained at a single-S vacancy ($V_s = -400$ mV, $I_t = 500$ pA, $V_{mod} = 0.5$ mV), which is highly reproducible with different samples and STM tips. The energy spacings are labeled as $\Delta 1$ and $\Delta 2$ in **(a)**. **b**, Yellow and the purple dots in the left panel represent the average energy spacing of $\Delta 1$ and $\Delta 2$, respectively. All the individual reproducible measurements are displayed in the right panel, indicating that the peak energies are equally spaced.



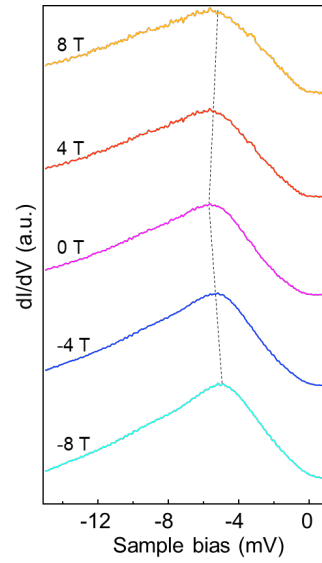
Extended Data Fig. 4 | Two peak feature of dI/dV spectra obtained on single S vacancy site. **a**, dI/dV spectra obtained on single S vacancy ranging from -300 mV to -200 mV, showing a two-peak feature near -283 mV ($V_s = -300$ mV, $I_t = 500$ pA, $V_{mod} = 0.5$ mV). **b**, The two sets of energy peaks show a similar variation of ± 1.5 mV, indicating that the bound states are robust at the single S vacancy site.



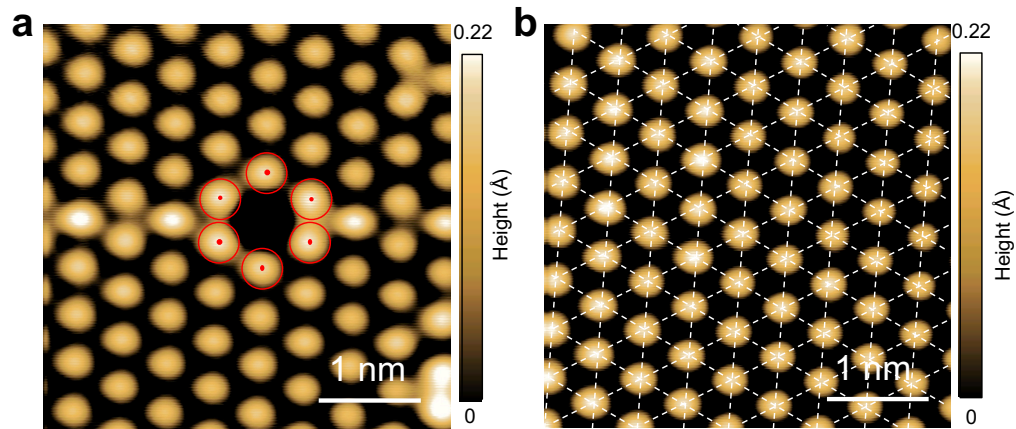
Extended Data Fig. 5 | The calculated electronic structure of S-terminated surfaces with a S vacancy (V_s). **a**, The band structures of the pristine S surface (in a 4×4 supercell). **b**, The band structure of S surfaces with a V_s . By comparing (**a**) and (**b**), the bound state was recognized and labeled by the blue arrow. **c**, Spin resolved DOS projected on the S vacancy. It is clearly shown that the S vacancy is spin polarized, which is in agreement with the experimental observation. **d**, Spin resolved DOS projected on the three Co atoms under the S vacancy. Comparing (**c**) and (**d**), we can conclude that the magnetic moment of V_s has the same direction as that of the Co_3Sn plane.



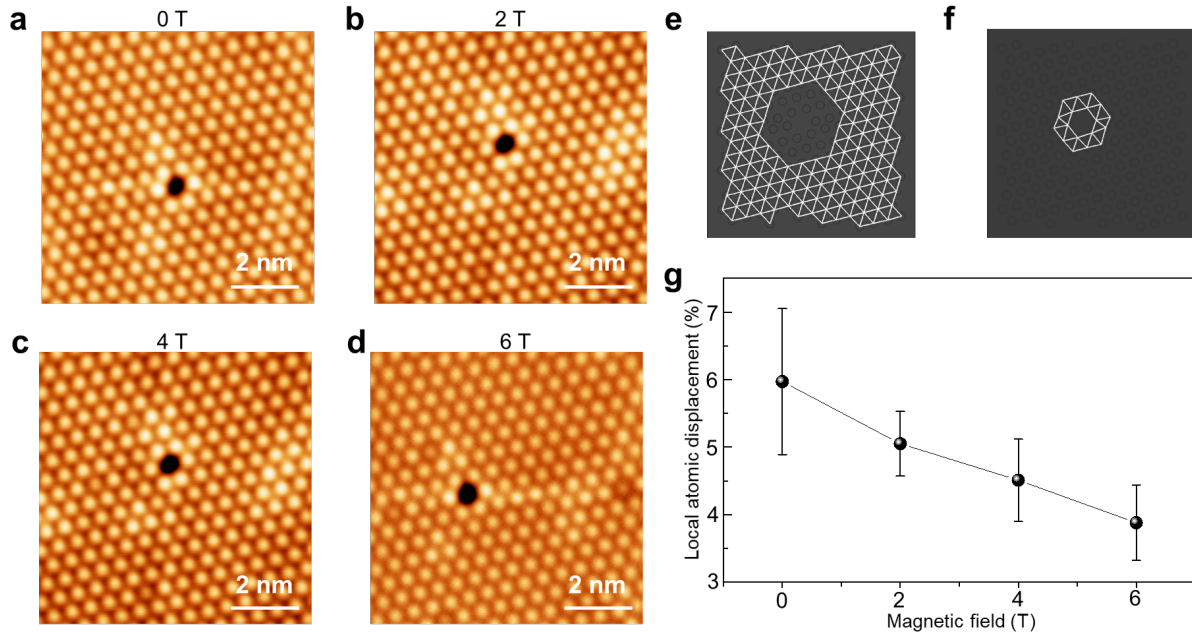
Extended Data Fig. 6 | Reproducibility on the other vacancies. **a**, Magnetic dependence of the peak positions on a single vacancy ($V_s = -400$ mV, $I_f = 500$ pA, $V_{mod} = 0.5$ mV). **b**, Intensity plot of the interpolated field-dependent spectra, showing a similar shift as that in (a). **c**, Energy shift as a function of magnetic field in (a).



Extended Data Fig. 7 | Magnetic dependence of Sn surface. The energy peak shifts towards higher energy with a slope of $165 \mu\text{eV/T} = 2.9 \mu_B$, which is in consistent with previous literature¹³ ($V_s = -400 \text{ mV}$, $I_t = 500 \text{ pA}$, $V_{mod} = 0.5 \text{ mV}$).



Extended Data Fig. 8 | STM images of single vacancy region and clean S region. a, Red circles and points represent the atom sites around the single vacancy. **b,** The white dashed lines display the lattice structure and atom sites of the intact region. ($V_s = -400$ mV, $I_t = 100$ pA).



Extended Data Fig. 9 | Statistic analysis of magnetic-field-dependent local atomic displacement of single S vacancy. **a-d**, STM images of single S vacancy obtained under 0 T (**a**), 2 T(**b**), 4 T (**c**) and 6 T (**d**), respectively ($V_s=-400$ mV, $I_f=100$ pA).. **e**, An example of statistics of nearest distances in the region far away from vacancy in (**c**). The average distance is thought to be the standard atom-atom distance \bar{d} . **f**, An example of statistics of nearest distances (d_i , $i=1, 2, 3, \dots, 36$) in the region of vacancy in (**c**), according to the dI/dV map of vacancy in Fig. 3c in the main text. The local atomic displacement of single S vacancy σ is defined as $\sigma = \frac{\sum_{i=1}^{36} |d_i - \bar{d}|}{36 \bar{d}}$. **g**, The local atomic displacement as a function of the value of magnetic field, showing that the displacement is inversely proportional to the value of magnetic field. The error bar come from the variation in the determination of atom position and calculations of nearest atom-atom distances.

References:

24. Kresse, G.; Furthmuller, J. Efficiency of ab-initio total energy calculations for metals and semiconductors using a plane-wave basis set. *Comput. Mater. Sci.* **6**, 15-50 (1996).
25. Kresse, G.; Furthmuller, J. Efficient iterative schemes for ab initio total-energy calculations using a plane-wave basis set. *Phys. Rev. B: Condens. Matter Mater. Phys.* **54**, 11169-11186 (1996).
26. Blochl, P. E. Projector augmented-wave method. *Phys. Rev. B: Condens. Matter Mater. Phys.* **50**, 17953-17979 (1994).
27. Perdew, J. P., Burke, K. Ernzerhof, M. Generalized gradient approximation made simple. *Phys. Rev. Lett.* **77**, 3865-3868 (1996).
28. Chen, H., Xiao, W., Wu, X., Yang, K. & Gao, H.-J. Electrochemically etched Ni tips in a constant-current mode for spin-polarized scanning tunneling microscopy. *J. Vac. Sci. Technology B Nanotechnol. Microelectron Mater. Process Meas. Phenom.* **32**, 061801 (2014).